

# A Dual-Band Spaceplate: Contracting the Volume of Quasi-Optical Systems

Michal Mrnka<sup>ID</sup>, Ian R. Hooper<sup>ID</sup>, Harry Penketh<sup>ID</sup>, David B. Phillips<sup>ID</sup>, and Euan Hendry<sup>ID</sup>

**Abstract**—A “spaceplate” approximates the angular response of free space with a much thinner nonlocal metamaterial. They have the potential to significantly shrink the volume of optical and quasi-optical systems, by allowing elements such as lenses to be moved closer together. However, spaceplates exhibit a tradeoff between their operational angular and spectral bandwidths. In this work, we present a new space-compression concept: a dual-band spaceplate capable of operating in two distinct frequency bands simultaneously. This allows the limited spectral bandwidth to be targeted to application-specific parts of the spectrum. Our design is composed of a multilayer stack of semitransparent mirrors separated by free-space voids. These layers act as a system of coupled Fabry–Pérot (FP) cavities—the guided-mode resonances of which emulate the effect of free-space propagation. The stack is engineered to exhibit two resonant subbands, with the frequency separation a tunable parameter in the design. We numerically and experimentally demonstrate a dual-band spaceplate exhibiting space compression at two distinct frequency subbands centered about 21.4 and 23.7 GHz.

**Index Terms**—Dual-band, electromagnetic metamaterials, Fabry–Pérot (FP) interferometers, wave propagation.

## I. INTRODUCTION

THE miniaturization of optical and quasi-optical [1] systems has, in the last decade, mainly involved research into reducing the size of bulk optical elements, such as lenses and mirrors, by replacing them with ultrathin metamaterials [2], [3]. In the microwave part of the electromagnetic spectrum, these components are best represented by the concepts of reflectarrays and transmitarrays (i.e., array lenses) [4], [5], [6], [7], [8]. Only recently, it was realized that the distances between optical elements can also be reduced, through novel approaches in the emerging field of nonlocal metamaterials [9], [10], [11]. The basic idea is to engineer

Manuscript received 9 May 2023; revised 28 July 2023 and 12 September 2023; accepted 19 October 2023. Date of publication 7 November 2023; date of current version 5 June 2024. This work was supported by the Engineering and Physical Sciences Research Council (EPSRC) under Grant EP/S036466/1. The work of Ian R. Hooper was supported in part by EPSRC and QinetiQ Ltd., via the TEAM-A Prosperity Partnership under Grant EP/R004781/1 and in part by EPSRC via under Grant EP/W003341/1. The work of Harry Penketh was supported in part by EPSRC and QinetiQ Ltd., via the TEAM-A Prosperity Partnership under Grant EP/R004781/1. The work of David B. Phillips was supported in part by the Royal Academy of Engineering and the European Research Council under Grant 804626. (Corresponding author: Michal Mrnka.)

The authors are with the Department of Physics and Astronomy, University of Exeter, EX4 4QL Exeter, U.K. (e-mail: m.mrnka@exeter.ac.uk).

Color versions of one or more figures in this article are available at <https://doi.org/10.1109/TMTT.2023.3328474>.

Digital Object Identifier 10.1109/TMTT.2023.3328474

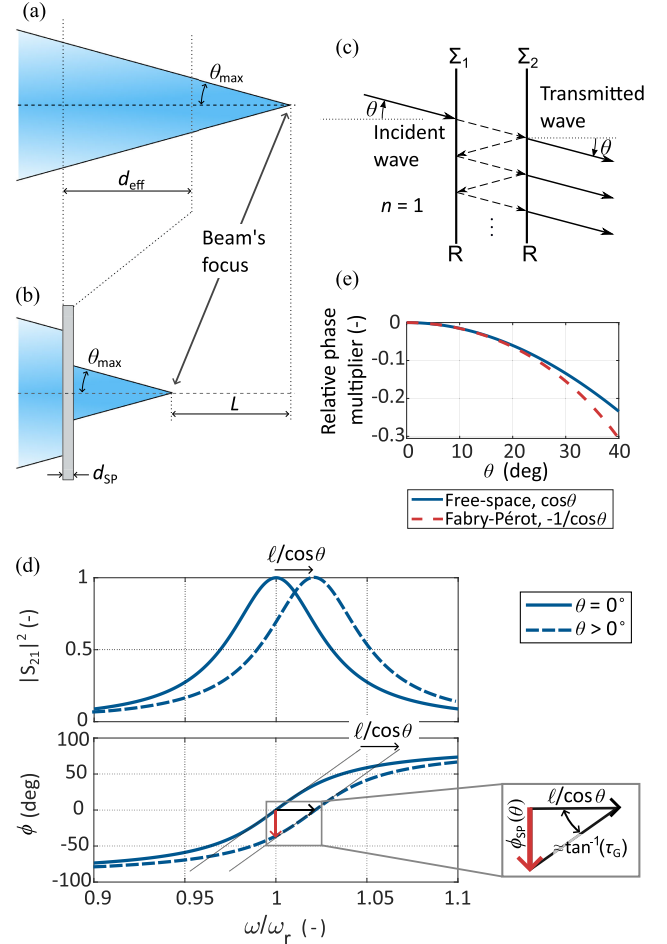


Fig. 1. (a) and (b) Principle of space compression. (a) Converging beam focuses at a certain location through free-space propagation. (b) Spaceplate is placed into the beam's path and the focus is shifted by a distance,  $L$ , without changing the convergence angle. (c) FP etalon formed from two partial mirrors with reflectances  $R$ . (d) Transmittance and transmission phase of an FP cavity close to a half-wavelength resonance as a function of angular frequency  $\omega$  for two incident angles. (e) Comparison of the functions  $\cos \theta$  and  $-1/\cos \theta$ , which are proportional to the phase of free space and of an FP cavity, respectively.

new passive components coined “spaceplates” [10], which are capable of replacing a slab of free space with a much thinner metamaterial, thus shrinking the axial dimensions of optical systems without any changes to the properties of propagating beams. This phenomenon is known as “space compression” or “space squeezing.”

A spaceplate is designed by tailoring the angular response of certain physical structures, as first proposed independently

in [10] and [12]. We can distinguish two families of spaceplates based on the design principles employed. First, *stochastic spaceplates* [10], [13], [14] rely on numerical optimization to design a multilayer stack of homogeneous, isotropic layers. The material properties and thicknesses of individual layers are optimized to reach an optical transfer function as close to the equivalent free space as possible. Second, *deterministic spaceplates* are designed by engineering the response of a known, deterministic structure that approximates the optical transfer function of free space, such as Fabry–Pérot (FP) cavities [14], [15], photonic crystals [12], [16], uniaxial media [10], and homogeneous materials with refractive index  $n$  smaller than the surrounding medium [10].

The main parameter that determines the performance of a spaceplate is its *compression factor*  $\mathcal{C}$  defined as a ratio of the thickness of the slab of free space that the spaceplate replaces  $d_{\text{eff}}$  to the thickness of the spaceplate itself  $d_{\text{SP}}$  (see Fig. 1)

$$\mathcal{C} = d_{\text{eff}}/d_{\text{SP}}. \quad (1)$$

Recently, several theoretical studies have been published exploring the limits of specific resonator-based spaceplate designs [14] and space-compression in general [11], [17]. Four metrics are tied together, which limits the performance of any spaceplate as demonstrated in [14]: compression factor, numerical aperture (angular range), frequency bandwidth, and transmission efficiency. There will always be a tradeoff between these metrics that must be considered in any design process. The improvement of one will inevitably lead to the deterioration of the others.

Radio and microwave systems, meanwhile, often operate at two distinct, well-separated, frequency bands. Such application areas include cellular and local (wi-fi) communication networks, automotive [18] and weather [19] radars, dual-frequency GNSS systems [20], [21], remote-sensing instruments [22], [23], and THz imaging [24], [25] to name a few. As increasing the bandwidth of a spaceplate comes at the expense of its compression factor, it is desirable to develop a spaceplate design capable of operating at two distinct narrowband frequencies. This would yield a high compression factor within each band and outperform the current alternative: a single broadband structure with lower compression over the entire spectral range.

In this article, we design and experimentally demonstrate the first dual-band spaceplate. We achieve dual-band operation using coupled resonances of two FP cavities. It is known that a single FP cavity shows a significant space-compression effect around its interference maxima [15]. By introducing a second, identical cavity, in the vicinity of the first, and by adjusting the separation distance between them to vary the coupling strength, we can split the resonance line into two sub-bands and tune their frequency separation. This results in two distinct pass bands, both of which exhibit space compression.

The concept of space compression is described in more detail in Section II, while in Section III- we investigate the dual-band structure numerically with cavities based on metal-mesh partial mirrors in the 20–25-GHz frequency range. In Section IV, we design an experimental dual-band

spaceplate based on meshes etched on PCB substrates and subsequently demonstrate its space compression properties in both frequency bands. In Section V, we discuss the systematic error introduced by the material under test during its free-space characterization and some practical limits of the design, before concluding the article in Section VI.

## II. FUNDAMENTALS OF SPACE COMPRESSION WITH AN FP CAVITY

The concept of space-compression can be illustrated by considering a simple scenario: a converging beam (i.e., a cone of light under the ray approximation) focusing to a point [see Fig. 1(a)]. A material or optical component invokes space compression when its introduction into the path of the beam causes the location of the focus to shift upstream along the axis, back toward the source [Fig. 1(b)]. The effect of a spaceplate can thus be considered the direct opposite of that of a dielectric slab of material, with a refractive index higher than the surrounding medium, introduced into the converging beam path [26]. In that case, the focal position of the beam is shifted along the axis, further away from the slab—optically increasing the size of the system.

The relevant properties of free space can be described by the optical transfer function  $H$  that accounts for diffraction, and the angle-dependent phase delay picked up by a single plane-wave component (i.e., Fourier component) propagating at an angle  $\theta$  with respect to the optical axis. In a free-space region with thickness  $d_{\text{eff}}$ , it follows that:

$$H(\theta) = \exp(ik d_{\text{eff}} \cos \theta) \quad (2)$$

where the free-space wavenumber  $k$  is given by  $k = 2\pi/\lambda$ , and  $\lambda$  is the wavelength. It follows that the magnitude of  $H$  is unity and independent of  $\theta$ . We note that in microwave engineering, the optical transfer function corresponds to the transmission coefficient or a scattering parameter  $H \equiv S_{21}$  defined between two reference planes (see Fig. 1(c)  $\Sigma_1$  and  $\Sigma_2$ ).

Ideally, to replace free space of a certain thickness with a thinner spaceplate, the transfer function of the spaceplate,  $H_{\text{SP}}$ , should exactly match that of the replaced free space. In reality, it is sufficient that the transmission magnitude  $|H_{\text{SP}}|$  is relatively flat across the angular range of interest ( $-\theta_{\text{max}}$  to  $\theta_{\text{max}}$ ), even if less than unity. Ensuring that all the angular components are attenuated by the same amount minimizes aberrations in the transmitted field. Evidently, the phase delay  $\arg(H_{\text{SP}})$  should approximate that of free space as closely as possible: it is the engineering of the angular phase response that is essential to achieving a distortion-free space-compression effect.

A single resonant mode FP cavity exhibits in transmission an angular phase dependency that is related to the shift of the resonance as a function of incident angle  $\theta$  and is given by [14]

$$\phi_{\text{SP}} = -\ell \frac{\tau_g}{\cos \theta} \quad (3)$$

where  $\tau_g = \pi Q/2\omega_r$  corresponds to the group delay of the resonator close to the resonance at normal incidence,

$Q$  is the quality factor,  $\omega_r = 2\pi f_r$  is the angular resonant frequency, and  $\ell$  is the order of the resonance (for constructive interference  $\ell = 1, 2, 3, \dots$ ).

The reason why an FP cavity approximates (for small angles) the transfer function of free space becomes clear upon expanding the angular dependent terms of the phase in their Taylor series. Considering free space in which the phase follows  $\cos \theta$  and can be written as:

$$\cos \theta \approx 1 - \frac{\theta^2}{2!} + \frac{\theta^4}{4!} - \dots \quad (4)$$

while the transmission phase associated with the shift in the resonance frequency [see Fig. 1(d)] of an FP resonator is proportional to

$$-\frac{1}{\cos \theta} \approx -1 - \frac{\theta^2}{2!} - \frac{5\theta^4}{4!} - \dots \quad (5)$$

The only relevant terms in these two expressions are those that depend upon  $\theta$ , since the constants 1 and  $-1$  correspond to global phase shifts that are identical for all components of the angular spectrum. Thus, in the small-angle approximation, it is sufficient to consider only the quadratic term, which is the same for both free space and the FP cavity.

### III. DUAL-BAND OPERATION

The mechanism proposed here to achieve dual-band operation is to bring two FP resonators tuned to the same resonant frequency into close vicinity of one another so that the resonant modes of the cavities couple together. As a result, the resonance line splits into two subbands whose separation in frequency can be tuned by altering the distance (i.e., coupling strength) between them [27]. The two distinct resonance peaks correspond to the modes with parallel and antiparallel electric field oscillations in the individual cavities formed by mirrors  $M_1M_2$  and  $M_3M_4$  and are symbolically depicted in Fig. 2(f). The central frequency is set by the resonant frequency of the isolated cavities, while the bandwidth of each of the subbands is influenced by their  $Q$  factors. In this work, the individual cavities are tuned to the lowest-order resonance resulting in constructive interference with electrical thickness  $\sim \lambda/2$ . Higher-order modes can be alternatively used at the expense of numerical aperture and bandwidth [14]. In place of the tunable gap size, control over the resonant frequencies could be introduced by unequal cavity thicknesses. However, the transmission efficiency is reduced due to lower coupling efficiency in this case.

A simplified schematic of our dual-band space compression structure is shown in Fig. 2(a). It is formed from two FP cavities separated by a distance  $g$ , with each cavity being composed of two identical partially reflective mirrors,  $M_1 - M_4$ . Here, the mirrors consist of metallic periodic hole arrays, whose reflectivity can be tuned by adjusting the ratio of the period to the hole size [see Fig. 2(b)] for a unit cell of the structure.

Numerical analysis is performed in Ansys HFSS for a unit-cell structure [Fig. 2(b)] defined by the following set of parameters reflectances of the PEC-based hole array mirrors  $R \approx 0.935$  ( $R = |S_{11}|^2$ ), period of the square lattice

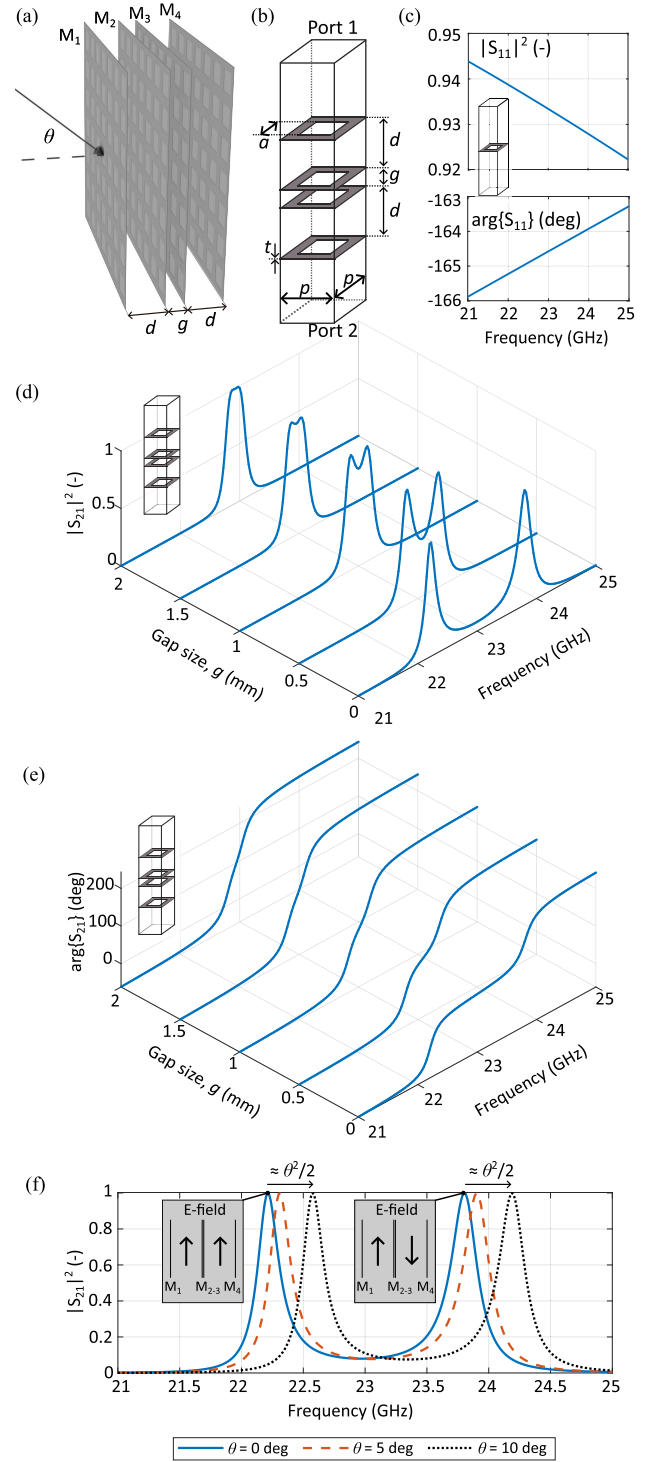


Fig. 2. (a) Geometry of the dual-band spaceplate—two cavities formed by mirrors  $M_1M_2$  and  $M_3M_4$  are separated by a coupling gap  $M_2M_3$ . (b) Schematic of the unit cell used for numerical analysis showing the period of the hole array structure,  $p$ , and the size of the holes,  $a$ . (c) Reflectance and the reflection phase of a single semitransparent mirror. (d) and (e) Normal incidence transmittance and transmission phase of the coupled cavities as the gap width  $g$  increases, showing the splitting of the resonance line. (f) Quadratic frequency shift of the resonances for increasing incident angle  $\theta$  and the electric field orientation inside individual cavities at the two resonances.

$p = 1.5$  mm, hole size  $a = 1.28$  mm, thickness of the mesh sheets  $t = 0.035$  mm, and distance between the mirror sheets



that form the resonators  $d = 6$  mm. The resonant frequency of an isolated cavity is at 22.91 GHz and the  $Q$  factor  $\approx 45$ .

The dependence of the coupling gap,  $g$ , on the frequency splitting of the coupled modes is shown in Fig. 2(d) and (e). We plot the transmittance, that is, the square of the magnitude of the transmission coefficient [Fig. 2(d)], and the phase of the transmission coefficient [Fig. 2(e)].

As the coupling gap shrinks, the splitting of the single resonance feature (corresponding to the FP resonance of the initially uncoupled cavities) increases. There is a small increase in the linewidth and reduction of the phase slope for the higher frequency resonance, and this is a result of the small frequency dependence of the reflectivity of the mirrors [see Fig. 2(c)]. As a result, the compression factor  $\mathcal{C}$  will be slightly smaller close to the second resonance. Crucially, in the small-angle approximation, the frequency of both resonances increases as a function of the incident angle  $\theta$  according to  $f_r \sim \theta^2$ . Given the linear behavior of the phase close to the resonance, this guarantees the space-compression operation of the structure in both frequency subbands.

It should be noted that the  $Q$ -factor of the individual cavities and the exact realization of the metal meshes (their surface inductance) have a strong influence on the maximum achievable separation between the bands. The higher the  $Q$ -factor, the more the fields are confined to the region between the cavity mirrors (i.e., regions with thickness  $d$ ), and for a given gap size the coupling between the cavities (and hence the degree of resonance splitting) decreases with increasing  $Q$ . Nevertheless, this effect has to be accounted for in any design methodology.

#### IV. EXPERIMENTAL DESIGN AND VALIDATION

##### A. Design

We design the partially reflective mirrors of the coupled-cavity spaceplate to be fabricated through a standard printed circuit board process. As a result, the metallic meshes are etched in the copper cladding of a microwave dielectric substrate Rogers R4350B [see Fig. 3(a)]. The substrate's thickness is 1.524 mm, dielectric constant  $\epsilon_r = 3.66$ , loss tangent  $\tan\delta = 0.0037$  (10 GHz), and copper cladding thickness  $35 \mu\text{m}$ . It is reasonable to assume that the dielectric loss in the operating frequency range ( $\sim 21$ – $24$  GHz) is somewhat higher than the value quoted by the manufacturer at 10 GHz.

We choose the compression factor of our design to be in the range 6–8. This value gives a substantial path length change that would be easy to observe in an experiment, while keeping the measurement artifacts due to defocusing at negligible levels. This compression factor corresponds to a maximum angle of incidence of approximately  $19^\circ$ – $22^\circ$ , considering monochromatic radiation and  $-3$ -dB transmission loss at normal incidence due to the tradeoff between different performance characteristics [14]. We can calculate the approximate required reflectance of the mirrors from the desired compression factor as

$$R \approx e^{-\pi/2\mathcal{C}}. \quad (6)$$

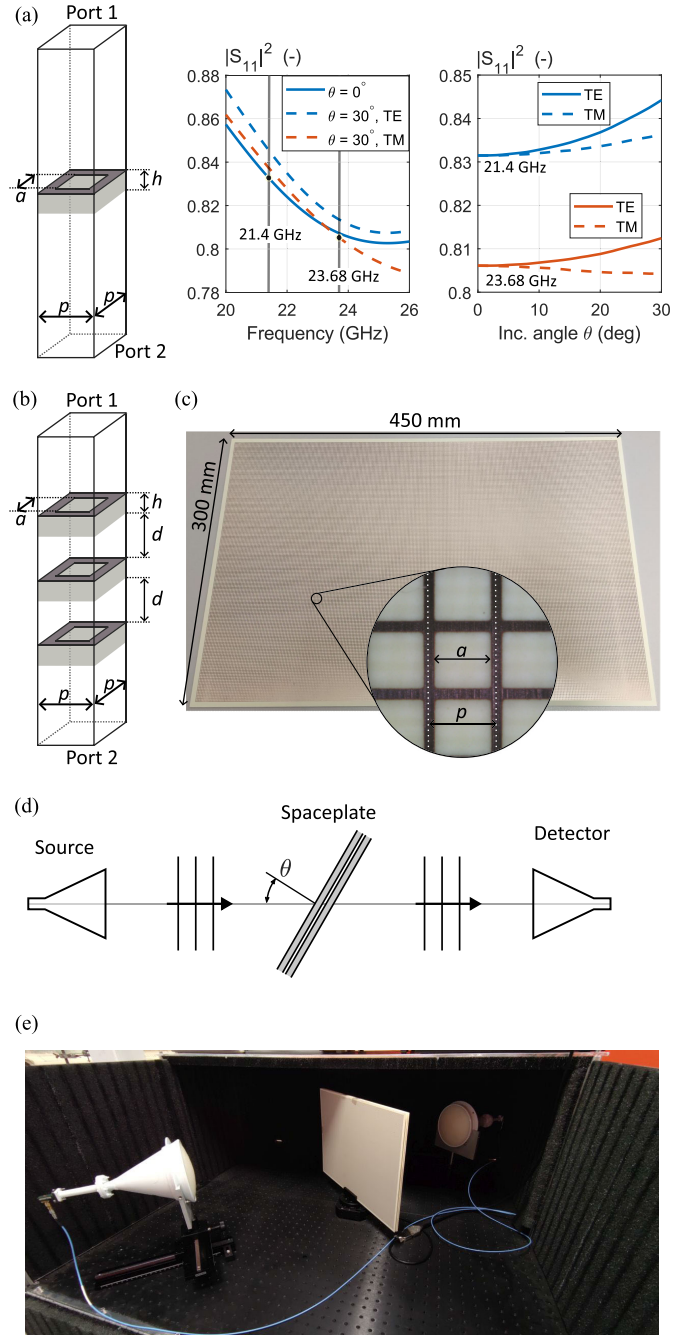


Fig. 3. (a) Unit cell of the mirror with its reflectance as a function of frequency and angle. (b) Unit cell of the designed spaceplate. (c) Fabricated hole-array mirror on a PCB. (d) Schematic view of the experimental setup. (e) Photograph of the setup with the spaceplate sample located between the horn antennas.

We note that this equation represents the theoretical limit. It relies on infinitely thin, lossless mirrors in free space (not those deposited on dielectric substrates). Therefore, in reality, the actual achievable compression factor is slightly lower.

The mirrors described in Section III are redesigned to include the dielectric substrates. The unit-cell model of the single mirror is given in Fig. 3(a) and of the whole spaceplate in Fig. 3(b). The final dimensions of the structure are: hole period  $p = 1.5$  mm and hole size  $a = 1.26$  mm. The resultant reflectance  $R$  (i.e.,  $|S_{11}|^2$ ) of individual mirrors as a function of

frequency for normal incidence and for incident angle  $\theta = 30^\circ$  is shown in Fig. 3(a). We can see that the response of the mirrors' reflectivity is not flat with frequency. Fig. 3(a) also shows the change in reflectance with increasing incident angle for TE and TM polarizations. The important implication of this is that the compression factor is also a function of frequency, maximum angular range, and polarization and thus will differ for the two principal polarization states TE and TM.

Since we wish to demonstrate dual-band operation, we aim for a geometry that provides the largest possible frequency splitting of the resonance—one with the coupling gap between the two resonators of 0 mm. This results in only three mirrors being required, since the two cavities share the middle mirror [see Fig. 3(b)] for the unit cell of the final structure.

The lateral size of the spaceplate is  $450 \times 300 \text{ mm}^2$ . The individual PCB sheets are separated by a distance of  $d = 3 \text{ mm}$  by 3-D printed spacers placed in the corners of the device. The separation of the sheets is reduced compared to the previous section as now the cavities are partly filled with the higher  $\epsilon_r$  material, the reduced separation distance thus compensates for this and keeps the electrical thickness of the cavities close to the values from the previous section. The overall thickness of the device is  $d_{\text{SP}} = 10.68 \text{ mm}$ . A photograph of the sheets is given in Fig. 3(c) and the sample is shown in the quasi-optical measurement setup in Fig. 3(e).

### B. Experimental Validation

In the experiment, we measure the angular and frequency dispersion of the space-compression sample in a free-space quasi-optical measurement setup in the frequency band 18–26 GHz and the angular range  $\pm 30^\circ$  from normal incidence. By comparing the measured transmission phase  $\arg\{S_{21}\}$  to the theoretical plane-wave phase in free space, we can quantify the amount of free space that has been compressed by the presence of the structure. The transmittance is then a measure of the transmission efficiency at a given frequency and angle.

The experimental setup is shown in Fig. 3(d). It comprises two lens-corrected horn antennas (Flann 810 series) with aperture diameter 150 mm, and with 3-dB beamwidths of  $5.7^\circ$  and  $6.6^\circ$  in the  $E$ - and  $H$ -planes, respectively. The midband gain of the antennas is 29.7 dBi. The antennas face each other and are connected to a vector network analyzer (Anritsu Vectorstar MS4647B). The distance between them is 1 m, and a computer-controlled rotation stage, which mounts the sample, is located in the middle between the antennas. To mitigate standing waves in the experimental setup, partially absorbing foam layers (ABS-Technics ABS-ASF-12) are placed in front of the antennas. These attenuate the spurious reflections between the apertures of the horns and the sample.

During the experiment, we measure the complex, normalized transmission coefficient  $S_{21}^{\text{norm}}$  given by

$$S_{21}^{\text{norm}} = \frac{S_{21,\text{Sample}}}{S_{21,\text{Ref}}} \quad (7)$$

where  $S_{21,\text{Sample}}$  represents the measured complex transmission coefficient with a spaceplate sample in between the horns,

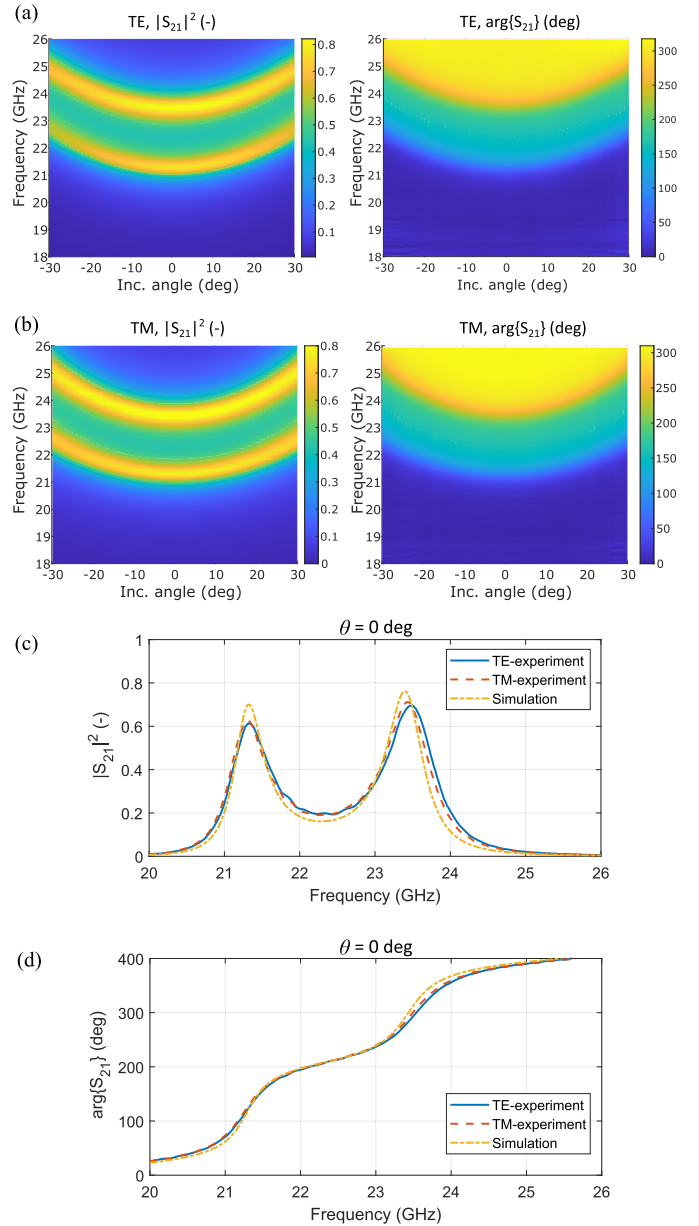


Fig. 4. Measured transmittance and transmission phase as functions of incident angle and frequency for (a) TE and (b) TM polarizations. (c) Measured transmittance and (d) transmission phase at normal incidence from two independent measurements compared to simulation results. Theoretically, the TE and TM polarization measurements should give identical results. In our case, the small difference is caused by the mounting repeatability of the spaceplate in the setup and a small beam divergence of the antennas.

and  $S_{21,\text{Ref}}$  is the reference transmission coefficient with the sample taken out. As a result of this quasi-optical calibration, the measured normalized phase is referenced to a slab of air (free space) with the same thickness as the spaceplate. To accurately judge the performance, we have to normalize the phase to a zero-thickness slab of free space [28]. We do this by multiplying the measured normalized  $S_{21}^{\text{norm}}$  with a factor  $e^{ik d_{\text{SP}} \cos \theta}$ , thus changing the reference path length for phase to 0 mm, neglecting the magnitude effects caused by the diffraction loss in the process. By doing so, we obtain a phase that corresponds to the analytical and numerical (HFSS)

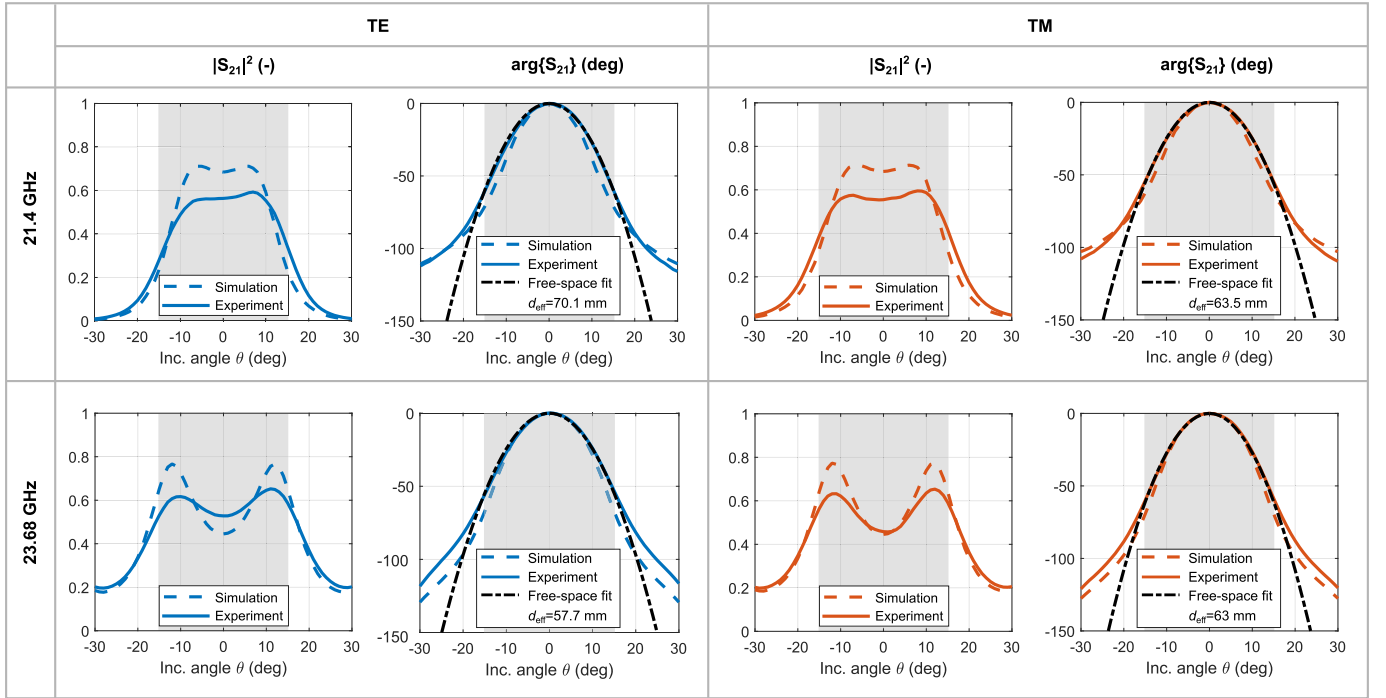


Fig. 5. Measured and simulated transmittance and transmission phase as a function of incident angle at two frequencies of operation 21.4 and 23.68 GHz and for two polarizations TE/TM. Solid lines represent experimental data and dashed lines simulation results from Ansys HFSS. Dashed-dotted lines in the phase plots represent free space that fits the measured phase patterns, hence the effective thickness of free space  $d_{\text{eff}}$  can be calculated. The gray regions in the plots highlight the angular range of operation  $\pm 15^\circ$ , where the phase of the spaceplate approximates well the free-space phase with a maximum error of  $1.5^\circ$  at the edges of the gray regions.

models

$$S_{21}(\theta, f) = e^{ik d_{\text{sp}} \cos \theta} \cdot S_{21}^{\text{norm}}(\theta, f). \quad (8)$$

### C. Measurement Results

The measured transmittance  $|S_{21}(\theta, f)|^2$  and transmission phase  $\arg\{S_{21}(\theta, f)\}$  for TE and TM polarizations are plotted in Fig. 4(a) and (b), respectively. The resonance line splitting into two subbands due to the coupling of the cavities is clearly seen on the transmittance plots. The quadratic-like increase of resonance frequency of both of the resonances as a function of the incident angle is clear and accompanied by the increased phase gradient close to each of the resonances. A 1-D frequency cut at normal incidence is shown in Fig. 4(c) and (d), alongside the simulation results obtained from the unit-cell modeling in Ansys HFSS. The lines corresponding to the experimental data in TE/TM polarization differ slightly as a result of the limited repeatability of the mechanical mounting of the sample. The simulations predicted slightly higher peak transmissions (at 21.3 GHz and 23.4 GHz), alongside a corresponding increase in the gradient of the transmission phase close to each resonance. Both effects can be traced to a reduced  $Q$ -factor of the cavities likely caused by higher dielectric losses in the mirror substrates compared to that used in the numerical model (taken from the data sheet for a lower frequency of 10 GHz), as well as from inhomogeneous broadening of the resonance lines due to uneven surfaces of the mirrors and a slightly diverging beam.

As we will show later, the maximum compression factor is obtained at frequencies somewhat higher than the

resonance peaks [15], in our case at 21.4 and 23.68 GHz. We plot the angle-dependent transmission and phase for these two frequencies in Fig. 5, with the approximate angular range of operation highlighted by the gray background. Experimental results are compared to simulations with reasonable agreement. We can see the increased modulation (higher loss) of the simulated transmittance near normal incidence at 23.68 GHz for both TE and TM cases. This is caused by the higher resonance frequency being slightly shifted in the experiment with respect to the simulations, which was traced to an uneven spacing between the mirrors in the experiment. The selected frequency 23.68 GHz is thus closer to the resonance in experimental data and further away in simulation results. The difference between the frequency of operation and the resonant frequency gives rise to the dip in transmission at normal incidence, with maximum transmission at normal incidence when the two frequencies coalesce.

The small reduction in transmission at the resonance peak for incident angles away from the normal incidence [Fig. 4(a) and (b)] was likely caused by a combination of two effects: a slight lateral beam walk-off and by a nonnegligible power leakage from the sides of the finite-size cavities.

### D. Extraction of Compression Factor $\mathcal{C}$ From the Phase Plots

The  $\arg\{S_{21}\}$  plots in Fig. 5 include, besides the simulated and measured phase profiles, the phase of an equivalent thickness of free space that the space-compression sample substitutes. In fact, the sample virtually prolongs the path length by  $L = d_{\text{eff}} - d_{\text{sp}}$ . It is evident, looking at the



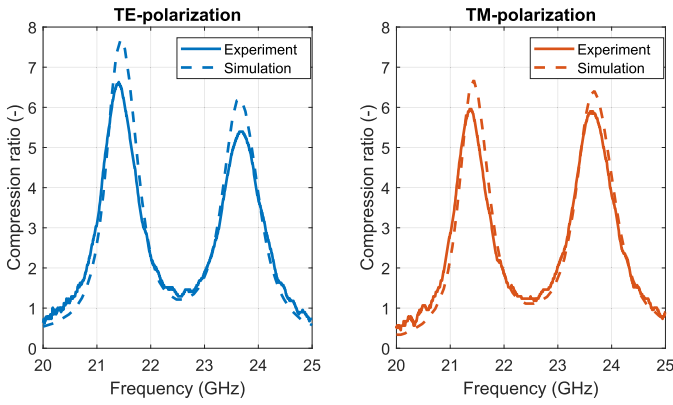


Fig. 6. Measured and simulated values of the compression factor as a function of frequency calculated using an angular range of  $\theta_{\max} = \pm 15^\circ$ .

phase plots, that within the angular range of operation, the sample approximates the effects of a much thicker slab of free space. For example, at 21.4 GHz, the 10.68-mm-thick sample approximates the properties of 70.1 mm of free space in TE and 63.5 mm in TM polarization. At the higher frequency point 23.68 GHz, the equivalent free-space distances for TE and TM polarizations are 57.7 and 63 mm, respectively.

The effective thickness of free space that the spaceplate replaces is determined by fitting a free-space dispersion (2) to the measured/simulated phase dispersion (see dashed-dotted lines in Fig. 5). This fitting is undertaken for each frequency over the range of angles corresponding to the operating range of the spaceplate, that is, numerical aperture  $NA = \sin \theta_{\max}$ , where  $\theta_{\max}$  represents the maximum incident angle accepted by the spaceplate. The result of the fitting is the distance  $d_{\text{eff}}$  and by knowing the thickness of the sample  $d_{\text{SP}}$ , we can evaluate the compression factor  $C = d_{\text{eff}}/d_{\text{SP}}$ . This is shown alongside compression factors obtained similarly from the simulated results in Fig. 6 and shows a small reduction in the maximum compression factor in the experiment due to additional losses not included in the simulations, for example, defocusing, inhomogeneous broadening, and higher dielectric losses in the microwave substrates.

## V. DISCUSSION

Here, we discuss some practical points related to the analysis, design, and experiments given in the previous sections. We focus on systematic errors in the measurement setup given by the nature of the space-compression sample and we highlight the frequency/polarization effects.

### A. Systematic Error Due to Defocusing

The experimental results presented in the previous section are not corrected for a systematic error caused by defocusing in the quasi-optical setup [29] introduced by the space-compression sample. This error results from the fact that the antennas' beams are slightly diverging. If a sample is introduced into the setup, the focusing conditions during the reference and sample measurements [see (7)] are not identical and additional terms have to be added to (7) (see [29]). In our setup, the different focusing conditions give rise to a

TABLE I  
OVERVIEW OF STATE-OF-THE-ART SPACEPLATES

Work	[10]	[10]	[14]	This work <sup>1</sup>
$C$ (-)	1.48	1.12	6	6 / 5.4
FBW (%)	-	69	6	3.4 / 2.1
$\theta_{\max}$	15	35	20	15 / 15
min. $T$ (%)	-	-	50	30 / 46
Background medium	Oil	Oil	Air	Air
<b>Number of bands</b>	<b>1</b>	<b>1</b>	<b>1</b>	<b>2</b>

loss mechanism that is related to the additional divergence of the beam over the path length that is virtually added to the measurement setup by the space-compression sample. We experimentally assessed the level of this loss, which is embedded in the results from the previous section, by increasing the distance between the horn antennas by a distance  $L = d_{\text{eff}} - d_{\text{SP}}$ , which corresponds to the distance effectively added by the sample. By comparing the transmittance between horns for the two configurations—original distance 1 m, and distance 1 m +  $L$ —we found that the additional loss amounted to no more than 3% of the peak value.

### B. Compression as a Function of Frequency and Polarization

In our design, we rely on hole arrays to form the mirrors of the space-compression cavities so that the structure can be designed in a tunable manner simply by optimizing the hole-to-period ratio. This leads to a frequency-dependent reflection from the mirrors [Fig. 3(a)], which in turn leads to a frequency-dependent compression factor. This becomes more pronounced as the frequency splitting between the two subbands increases. This effect could be mitigated through the use of dual-band frequency selective surfaces designed to give the desired reflection coefficient at the two subbands.

The polarization dependency of the compression factor originates from the Fresnel reflection coefficients at the mirrors, with TE polarization showing slightly higher reflection and thus the compression factor.

### C. Comparison to State-of-the-Art

As the field of space-compression optics has been established very recently [10], there are only a few designs that have been experimentally demonstrated. Since our structure represents the first dual-band spaceplate proposed thus far, we compare the properties in each of the bands to the performance of other spaceplates from the open literature in Table I. We focus on the following metrics: compression factor  $C$ , fractional bandwidth (FBW), maximum angle of operation  $\theta_{\max}$ , and minimum transmittance across the band ( $T$ ). The two spaceplates proposed in [10] rely on uniaxial crystal and negative index material and achieve compression factors of 1.48 and 1.12, respectively. However, both these designs require linseed oil as a background medium for operation, whereas the structure proposed in this article operates in air/free

<sup>1</sup>The values for the individual bands are separated by “/” symbol.

space. The single-cavity/single-band FP spaceplate [14] shows higher angular operating range, bandwidth, and higher transmission with comparable compression factor compared to each of the two bands of the dual-band structure proposed here. It is clear that the introduction of the second band comes at the cost of the performance.

## VI. CONCLUSION

A dual-band device (spaceplate) capable of approximating free-space propagation and thus shrinking quasi-optical systems has been proposed. It derives its function from two coupled FP cavities and from the resonance splitting that accompanies the coupled condition. By controlling resonance frequency and the level of coupling the frequencies of the subbands can be tuned. The designed spaceplate, with a 10.7-mm thickness, was capable of mimicking between 60 and 70 mm of free space depending on the frequency and polarization states. The performance was numerically studied and experimentally verified.

The dual-band concept can be extended straightforwardly for a higher number of subbands, simply by adding additional cavities. For example, a tri-band structure can be obtained by adding a third resonator to the dual-band structure or by making the size of the coupling gap large enough to support its own resonance at the desired frequency. However, for sufficient control over the central frequencies of the subbands, the structure would have to be asymmetric and the design/optimization process would be more challenging.

## ACKNOWLEDGMENT

For the purpose of open access, the author(s) has applied a Creative Commons Attribution (CCBY) license to any Accepted Manuscript version arising.

## REFERENCES

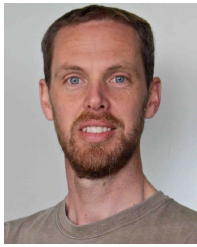
- [1] P. F. Goldsmith, *Quasioptical Systems: Gaussian Beam Quasioptical Propagation and Applications*. Hoboken, NJ, USA: Wiley, 1998.
- [2] J. B. Pendry, "Negative refraction makes a perfect lens," *Phys. Rev. Lett.*, vol. 85, no. 18, pp. 3966–3969, Oct. 2000.
- [3] V. M. Shalaev, "Optical negative-index metamaterials," *Nature Photon.*, vol. 1, no. 1, pp. 41–48, Jan. 2007.
- [4] D. Berry, R. Malech, and W. Kennedy, "The reflectarray antenna," *IEEE Trans. Antennas Propag.*, vol. AP-11, no. 6, pp. 645–651, Nov. 1963.
- [5] F. Li et al., "Generation and focusing of orbital angular momentum based on polarized reflectarray at microwave frequency," *IEEE Trans. Microw. Theory Techn.*, vol. 69, no. 3, pp. 1829–1837, Mar. 2021.
- [6] W. Zhang, H. Gomez-Sousa, J. Heredia-Jueas, and J. A. Martinez-Lorenzo, "Single-frequency imaging and material characterization using reconfigurable reflectarrays," *IEEE Trans. Microw. Theory Techn.*, vol. 69, no. 7, pp. 3360–3371, Jul. 2021.
- [7] A. H. Abdelrahman, A. Z. Elsherbeni, and F. Yang, "Transmission phase limit of multilayer frequency-selective surfaces for transmitarray designs," *IEEE Trans. Antennas Propag.*, vol. 62, no. 2, pp. 690–697, Feb. 2014.
- [8] I. Derafshi and N. Komjani, "A new high aperture efficiency transmitarray antenna based on Huygens metasurfaces," *IEEE Trans. Antennas Propag.*, vol. 70, no. 7, pp. 5458–5467, Jul. 2022.
- [9] K. Shastri and F. Monticone, "Nonlocal flat optics," *Nature Photon.*, vol. 17, no. 1, pp. 36–47, Dec. 2022.
- [10] O. Reshef et al., "An optic to replace space and its application towards ultra-thin imaging systems," *Nature Commun.*, vol. 12, no. 1, pp. 1–8, Jun. 2021.
- [11] D. A. B. Miller, "Why optics needs thickness," *Science*, vol. 379, no. 6627, pp. 41–45, Jan. 2023.
- [12] C. Guo, H. Wang, and S. Fan, "Squeeze free space with nonlocal flat optics," *Optica*, vol. 7, no. 9, pp. 1133–1138, Sep. 2020.
- [13] J. T. R. Pagé, O. Reshef, R. W. Boyd, and J. S. Lundeen, "Designing high-performance propagation-compressing spaceplates using thin-film multilayer stacks," *Opt. Exp.*, vol. 30, no. 2, pp. 2197–2205, Jan. 2022.
- [14] M. Mrnka et al., "Space squeezing optics: Performance limits and implementation at microwave frequencies," *APL Photon.*, vol. 7, no. 7, Jul. 2022, Art. no. 076105.
- [15] A. Chen and F. Monticone, "Dielectric nonlocal metasurfaces for fully solid-state ultrathin optical systems," *ACS Photon.*, vol. 8, no. 5, pp. 1439–1447, May 2021.
- [16] Y. J. Guo, M. Ansari, R. W. Ziolkowski, and N. J. G. Fonseca, "Quasi-optical multi-beam antenna technologies for B5G and 6G mmWave and THz networks: A review," *IEEE Open J. Antennas Propag.*, vol. 2, pp. 807–830, 2021.
- [17] K. Shastri, O. Reshef, R. W. Boyd, J. S. Lundeen, and F. Monticone, "To what extent can space be compressed? Bandwidth limits of spaceplates," *Optica*, vol. 9, no. 7, pp. 738–745, Jul. 2022.
- [18] X. Yi et al., "A 24/77 GHz dual-band receiver for automotive radar applications," *IEEE Access*, vol. 7, pp. 48053–48059, 2019.
- [19] H. Huang, K. Zhao, P. Fu, H. Chen, G. Chen, and Y. Zhang, "Validation of precipitation measurements from the dual-frequency precipitation radar onboard the GPM core observatory using a polarimetric radar in South China," *IEEE Trans. Geosci. Remote Sens.*, vol. 60, 2022, Art. no. 4104216.
- [20] (Jan. 2020). *Market Understands Value of Dual Frequency*. [Online]. Available: <https://www.euspa.europa.eu/newsroom/news/market-understands-value-dual-frequency>
- [21] J. Seo and T. Walter, "Future dual-frequency GPS navigation system for intelligent air transportation under strong ionospheric scintillation," *IEEE Trans. Intell. Transp. Syst.*, vol. 15, no. 5, pp. 2224–2236, Oct. 2014.
- [22] L. Bruckner, G. De Amici, E. Dinnat, D. Le Vine, and J. Piepmeyer, "A multi-band passive radiometer for sea salinity, soil moisture and cryosphere studies," in *Proc. IEEE Int. Geosci. Remote Sens. Symp.*, Jul. 2019, pp. 8909–8912.
- [23] F. Vanin et al., "Copernicus imaging microwave radiometer (CIMR): System aspects and technological challenges," in *Proc. IEEE Int. Geosci. Remote Sens. Symp.*, Sep. 2020, pp. 6535–6538.
- [24] W. Li et al., "Dual-color terahertz spatial light modulator for single-pixel imaging," *Light, Sci. Appl.*, vol. 11, no. 1, pp. 1–10, Jun. 2022.
- [25] P. Dean et al., "Dual-frequency imaging using an electrically tunable terahertz quantum cascade laser," *Opt. Exp.*, vol. 17, no. 23, pp. 20631–20641, Nov. 2009.
- [26] S. Nemoto, "Waist shift of a Gaussian beam by plane dielectric interfaces," *Appl. Opt.*, vol. 27, no. 9, p. 1833, May 1988.
- [27] J.-S. G. Hong and M. J. Lancaster, *Microstrip Filters for RF/Microwave Applications*. Hoboken, NJ, USA: Wiley, 2001.
- [28] G. L. Friedsam and E. M. Biebl, "A broadband free-space dielectric properties measurement system at millimeter wavelengths," *IEEE Trans. Instrum. Meas.*, vol. 46, no. 2, pp. 515–518, Apr. 1997.
- [29] M. Mrnka, R. Appleby, and E. Saenz, "Accurate S-parameter modeling and material characterization in quasi-optical systems," *IEEE Trans. THz Sci. Technol.*, vol. 12, no. 2, pp. 199–210, Mar. 2022.



**Michal Mrnka** received the Ing. (M.Sc.) and Ph.D. degrees in electronics and communications from the Brno University of Technology, Brno, Czechia, in 2013 and 2017, respectively. In his doctoral thesis, he focused on higher-order mode dielectric resonator antennas and analysis of perforated dielectrics in microwave applications.

Between 2015 and 2017, he worked as a Lead Antenna Engineer at ERA a.s., Pardubice, Czechia, developing antennas for passive multilateration surveillance systems. In 2017, he joined the European Space Research and Technology Centre, European Space Agency, Noordwijk, The Netherlands, where he was involved in instrumentation for (sub-)millimeter-wave material characterization and compact antenna test range measurements. He is currently a Research Fellow with the University of Exeter, Exeter, U.K., working on microwave and terahertz computational imaging.





**Ian R. Hooper** received the B.Sc. and Ph.D. degrees in physics from the University of Exeter, Exeter, U.K., in 1998 and 2002, respectively.

From 2002 to 2014, he was a Research Fellow investigating the interaction of electromagnetic and acoustic waves with materials. In 2014, he became the Technical Director of the EPSRC Centre for Doctoral Training in Metamaterials, University of Exeter, before becoming a Senior Research Fellow in 2018. His current research is focused on the design and experimental characterization

of metamaterials throughout the electromagnetic spectrum, particularly reconfigurable metamaterials.



**Harry Penketh** received the M.Phys. and Ph.D. degrees in physics from the University of Exeter, Exeter, U.K., in 2016 and 2021, respectively.

During this time, his work covered imaging in scattering media, phosphors for solid-state lighting, and computational imaging. He is currently a Research Fellow with the University of Exeter working on microwave and terahertz computational imaging.



**David B. Phillips** received the M.Sci. degree in physics from Durham University, Durham, U.K., in 2004, and the Ph.D. degree in nano-physics from the University of Bristol, Bristol, U.K., in 2012.

He worked in the defense industry as a systems engineer for three years. This included several months on a secondment to the U.K., parliament working at the Parliamentary Office of Science and Technology. After a short Post-Doctoral position at the Amolf Institute, Amsterdam, he returned to the U.K., in 2006, taking up an RCUK Fellowship at the University of Exeter. He is currently a Professor of ultrafast physics with the School of Physics and Astronomy, University of Exeter, Exeter, U.K. His current research focuses on imaging in the THz band and the design and application of low-frequency metasurfaces.

Dr. Phillips was awarded a five-year Royal Academy of Engineering Research Fellowship in 2016 and joined the University of Exeter in 2017 to establish his own research group. In 2018, he was awarded a five-year European Research Council Starting Grant (PhotUntangle), which currently mainly funds his group's activities.



**Euan Hendry** received the M.Sci. degree in chemical physics from the University of Glasgow, Glasgow, U.K., in 2000, and the Ph.D. degree in THz spectroscopy from the University of Amsterdam, Amsterdam, The Netherlands, in 2005.

After a short post-doctoral position at the Amolf Institute, Amsterdam. He is currently a Professor of ultrafast physics with the School of Physics and Astronomy, University of Exeter, Exeter, U.K. He returned to the U.K., in 2006, taking up an RCUK Fellowship at the University of Exeter. His

current research focuses on imaging in the THz band and the design and application of low-frequency metasurfaces.

Dr. Hendry was awarded an EPSRC Fellowship in 2012 and offered the Chair in ultrafast physics, Exeter, in 2017.